Blazed photon sieve for the correction of presbyopia

O Kummer, F Ogor, F Castignoles, J-L de Bougrenet de la Tocnaye, V Nourrit

Research Article Vol. 32, No. 1 / 1 Jan 2024 / Optics Express 396
Optics EXPRESS

Blazed photon sieve for the correction of presbyopia

O. KUMMER,[1,2,3] F. OGOR,[1] F. CASTIGNOLES,[2] J.-L. DE BOUGRENET DE LA TOCNAYE,[1,3] AND V. NOURRIT[1,3,*]

[1]IMT Atlantique Optics department, 29280 Brest, France
[2]Cristalens Industries, 22300 Lannion, France
[3]LaTIM, INSERM UMR1101, 22 Avenue Camille Desmoulins, 29200 Brest, France
[*]vincent.nourrit@imt-atlantique.fr

Abstract: What we believe to be a new type of transparent photon sieve is presented with application for presbyopia correction. Inspired by blazed gratings, we propose to design an intracorneal implant with slanted holes. The slopes introduce a new degree of freedom, breaking the symmetry of energy distribution along the optical axis and allowing to balance the energy between near and far vision. This new implant design is presented together with the simulation, manufacturing and validation methods. The first experimental results obtained with an implant manufactured in a biocompatible material are presented confirming the potential of the approach.

1. Introduction

Presbyopia is the progressive loss of ability to correctly accommodate on close objects. It is an unavoidable phenomenon linked to the loss of elasticity of the crystalline lens with age, and affects the entire population. The number of people in the world affected by presbyopia was estimated at 1.8 billion in 2015 [1].

There is currently no accepted solution to restore the accommodative function of the lens, but the loss of accommodation can be partially compensated by different optical techniques such as monovision: one eye is corrected for near vision, the other for distance vision and the oculo-cerebral system selects the sharp image [2]; multifocality: the eye is corrected for 2-3 precise distances thanks to a multifocal profile (introduced for example by contact lenses, intraocular implants or induced on the cornea by photo-ablation) [3–5]; or by increasing the depth of field whether with an approach similar to the multifocal approach [6]; or by pupil reduction [7].

Among the various methods used to implement the correction techniques listed above, corneal implants are still an underdeveloped solution [8,9], due in part to the difficulty of meeting the biocompatibility constraints specific to the cornea. They present however several advantages over existing solutions: they can eliminate the need for lenses or glasses and most importantly, unlike laser surgery, they are non-definitive solutions (no tissue is removed, which preserves the integrity of the cornea for other future options) and can be removed. This is especially important since presbyopia is a progressive loss of near vision.

Current intracorneal implants can be grouped into three categories depending on the approach used to modify the optical power of the eye. The implant can act solely by changing the curvature of the cornea [10]; have a power of its own combined by a change in corneal curvature [11]; or, as mentioned above, increase the depth of field by reducing the pupil diameter [12,13]. However, regardless of the category, an important constraint is that the implant does not negatively disrupt the passage of nutrients and waste products through the cornea [14].

In this context, Furlan et al [15,16], suggested the use of micro drainage holes (as already used in the implant Kamra) [17] but using a photon sieve (PS) structure [18,19] so that these holes do not degrade the imaging process but instead bring some multifocality. However, a limitation with this approach is the fact that such an implant, due to its geometry, will only create two opposite

#509300 https://doi.org/10.1364/OE.509300
Journal © 2024 Received 13 Oct 2023; revised 7 Nov 2023; accepted 8 Nov 2023; published 19 Dec 2023

Optics EXPRESS

foci with the same energy distribution. This means that it is not possible to modulate the axial energy distribution for greater visual comfort (an accepted requirement of visual comfort is a distribution between near and far vision of the order of 40/60%) [20].

In order to overcome this limitation on the distribution of energy in these foci, we sought to optimize a more complex hole profile based on the use of slanted holes. Although a large variety of holes pattern and distribution have been studied (e.g. fractal [21], Fibonnaci [22], or antihole [23]) and that the use of transparent multilevel has been suggested to improve diffraction efficiency, the customization of the 3D hole profile to control the amount of energy in the different orders has not been (to our knowledge) investigated. Our assumption is that with slanted holes, the holes can still allow nutrients to pass through but the slopes introduce a new degree of freedom that allows breaking the symmetry of light energy distribution for better visual comfort.

In this paper, we present this innovative design as well as experimental results validating our approach. This is to our knowledge, the first report of experimental results obtained with an intracorneal implant manufactured in a biocompatible material and based on the photon sieve principle. This paper is divided as follow. In the first section, the implant design is presented together with the simulation, manufacturing and validation methods. In the second section, experimental results are presented and compared to simulations. The last section discusses the benefits and potential impact of the proposed design.

2. Methods

2.1. Photon sieve design and simulations

The implant design is based on the principle of transparent photon sieves [24]. Photon sieves (PS) consists basically of a Fresnel zone plate where concentric holes are distributed over the open zones (Fig. 1). In a standard design, holes are arranged on a circle of radius

$$R_n = \sqrt{2nf\lambda + n^2\lambda^2} \tag{1}$$

with n the number of the ring, f the focal length of the photon sieve and lambda the wavelength. The associated phase profile makes it possible to obtain constructive interferences in 2 foci.

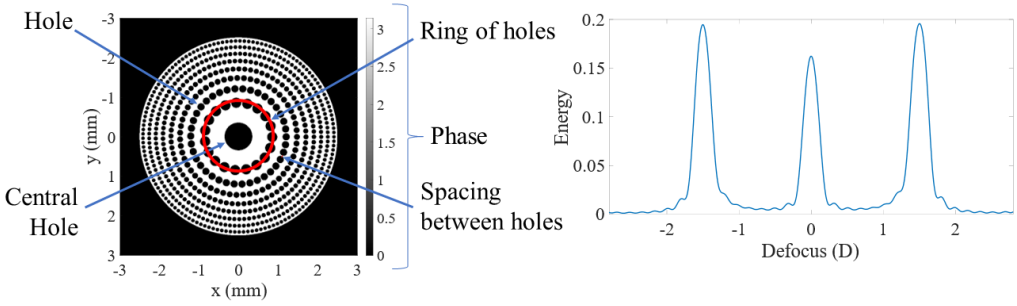

Fig. 1. Left: Holes distribution for a standard photon sieve and associated through focus energy (right) in a 60D eye. The PS thickness is chosen to produce a π-phase shift between the plain and holed part (respectively the white and black part in the left image). The central hole and the smallest holes are respectively 700 and 25 microns large in diameter. Right: energy (ES) distribution as a function of defocus. The central peak corresponds to the light that goes through the implant without forming interference (order 0), and the left and right peak correspond respectively to the -1 and +1 order.

In this paper, in order to have a convenient metrics to analyze the focusing properties of the PS, we use the encircled Strehl ratio (ES) defined as the ratio of the encircled energy of the PSF

Optics EXPRESS

within the first ring of the airy disk, over the diffraction limited encircled energy (for sake of simplicity, we denote it energy in the figures). The focal length chosen to calculate the Airy disc is the one of the eye (60D) (this corresponds to the case where the intracorneal implant only brings additional power for intermediate and near vision).

As a binary phase grating, a standard photon sieve is not well suited for the correction of presbyopia since the same amount of energy is distributed in the first orders (+1 and -1) whereas it is preferable to have more energy for far vision than near vision. Drawing inspiration from blazed gratings we propose to use slanted holes to break the energy distribution symmetry along the optical axis. The geometry of these slanted holes is presented in Fig. 2(b) next to the one of a standard hole Fig. 2(a). As depicted in Fig. 2 the hole is not just a tilted cylindrical hole but rather a cylindrical hole with a slanted "side". However, for sake of simplicity, we use in this paper the terms "blazed" or "slanted".

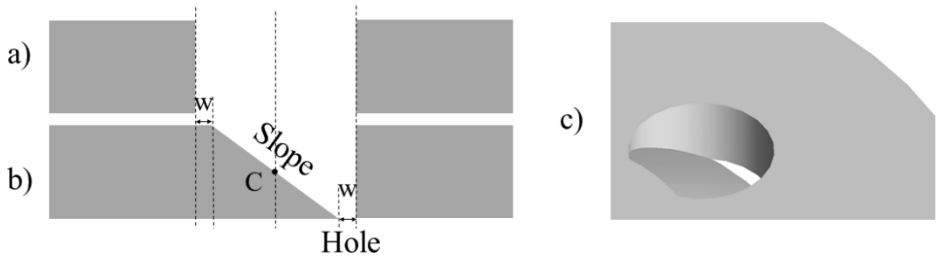

Fig. 2. (a) cross section-view of a regular hole; (b) cross section-view of a slanted hole; (c) CAD representation of a slanted hole.

The slope in Fig. 2(b) is defined so that its center (C) is positioned at R_n (in agreement with Eq. (1)) and that the width (w) of the through hole portion corresponds to a fraction of the width of a regular hole.

In addition, if we denote D the diameter of a regular hole Fig. 2(a) and (t) is the thickness of the implant the slope's steepness (θ) is given by :

$$\tan\theta = \frac{t}{D-2w} \tag{2}$$

The inclination of the slope therefore depends on three parameters: the size of the perforated zone (w), the implant's thickness (t) and the size of the holes (D).

The choice of (w) is a compromise between having a not too steep slope and a large enough perforated area. In this study we chose a value of 10%. If we consider a PS such as the one described by Furlan et al. [15], the smallest hole has a diameter of 100 microns, so in our case, the smallest "perforated" area would still be much larger than the nutrients molecules.

With regards to the implant's thickness, the slanted configuration, in addition to providing an additional parameter to control the energy distribution in the diffraction orders, also provides greater flexibility in the choice of implant thickness which is key for efficient manufacturing. In a standard PS, the implant thickness must be chosen so that the holes produce a π phase shift. In the slanted configuration, the implant thickness can be chosen for instance to produce a 2π phase shift. This has various advantages. First, with such a configuration, it is theoretically possible to add straight holes anywhere to achieve additional drainage capacity without changing the optical power of the implant. Second, for the same reason, the size of the central hole has almost no impact on light distribution (whereas the size of the central hole, for implants introducing a π phase shift, is optimal when it is the size of the first ring of the Fresnel lens). Third, the greater thickness facilitates the implant manufacturing. For instance, a 2π phase shift for an implant in Ormocomp (n = 1.52) placed into the cornea (n = 1.376) requires a thickness of 3.8 microns (for comparison, the Kamra implant is 6 microns thick).

Optics EXPRESS

Having defined the holes' radial positions (R_n), their height (2π) and the slopes geometry, we define its width as a function of K where K is defined as the ratio between the hole diameter (i.e. D_n, the hole including the slope, not just the perforated area, for the hole on the nth ring) and the width of the Fresnel zone [Eq. (3)] where it is positioned [19].

$$K = \frac{D_n\sqrt{2n}}{\sqrt{\lambda f}} \tag{3}$$

Finally, we consider a fixed spacing between consecutive holes on a given ring and denote it S. If K is fixed, the value of S thus sets the number of holes and consequently, the energy ratio between near/intermediate and far vision (since it directly defines the slope according to Eq. (2)). Please note that with a classic photon sieve, far intermediate and near vision would respectively correspond to the -1, 0 and 1st order. With our blazed PS, we can adjust the energy distribution in the different orders to minimize the energy in the -1 order and to use respectively the orders 0,1 and 2 for far, intermediate and near vision.

In order to assess the slanted PS performances for different values of K and S, the axial energy distribution produced by the sloped PS was calculated with MATLAB using the angular spectrum method at 546 nm. Since the implant is meant to be set in a human eye and to facilitate the analysis of the 0-order, a phase factor representing an ideal thin lens of 60D was added to the implant. We first optimized a simple configuration with regular holes and checked that our results corresponded to the classic photon sieve configuration. In agreement with literature, the amount of energy in the near and far vision is then proportional to the number of holes, and the energy distribution between the different orders can be controlled by the holes' diameters. In classic photon sieve choosing holes 40 µm apart, and whose size is equal to the corresponding Fresnel zone width, allows to maximize and distribute approximately equally the energy in the order 0 and first orders.

In the case of the slanted PS, the energy distribution depends on the same parameter but with a different impact on vision since different orders are used (i.e. 0,1,2 instead of -1,0,1). As with the classic PS, the holes' size (K) control the energy distribution in the different orders (one can view the photon sieve as a mask over a zone plate: when K varies, the part of the illuminated zone plate varies, and thus the interference pattern). Also, the more holes, the more energy is diffracted, thus increasing the energy for near/intermediate vision (in order to better assess the interest of the proposed PS for the correction of presbyopia, a 60D power was added to the PS to take into account the eye's refractive power). This is illustrated in Fig. 3 that represents the impact of K and S on the energy in the different orders.

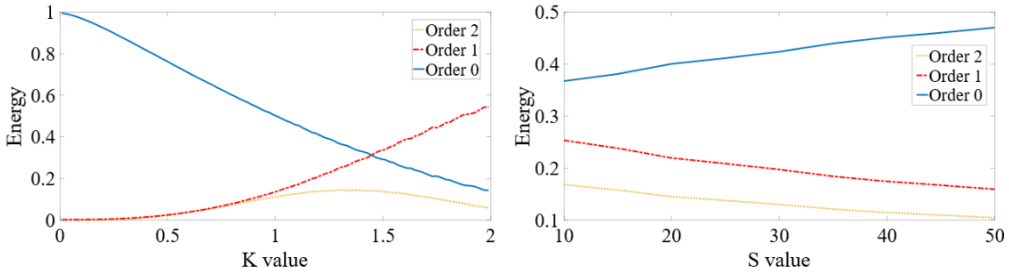

Fig. 3. Amount of energy (ES) in the 0th, 1st and 2nd order, i.e. respectively far (solid blue line), intermediate (dashed-dotted red line) and near vision (dotted orange line) as a function of holes size (K, for S = 25 µm, left image) and as a function of holes spacing (S, for K = 1.2, right image).

According to Fig. 3 a value of $K = 1.2$ allows maximizing the energy in the 2nd order while minimizing the difference with the first order, while a value of S = 35 µm allows to respect the

Optics EXPRESS

60% rule between far and near/intermediate vision. The through focus performances for such slanted PS are presented in Fig. 4 (phase screen representation and resulting light distribution). Sixty percent of energy is in the zero order (corresponding to far vision) and the -1 order (left of the 0 order in Fig. 4) is almost entirely suppressed which allows using the first and second order respectively for intermediate and near vision.

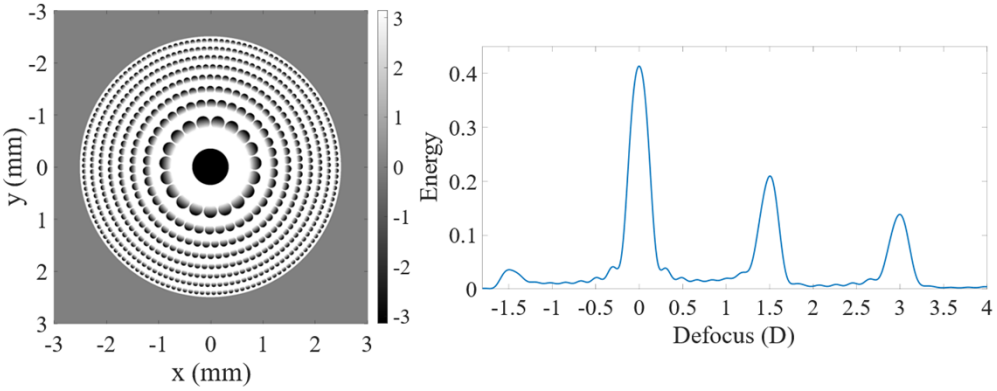

Fig. 4. Left: Holes distribution for the blazed photon sieve and associated through focus energy (right) in a 60D eye. The PS thickness is chosen to produce a 2π -phase shift between the plain and holed part. In the right image, the higher peak corresponds to the light that goes through the implant without forming interference (order 0), and the rights peaks correspond to the +1 and +2 order, that can be used respectively for intermediate and near vision.

The photon sieve being a diffractive element, chromatic aberrations are inevitably present. These aberrations will be opposed to the refractive ones. Repeating the calculation at 420 and 660 nm show that the chromatic aberrations for order 1 and 2 are respectively equal to -0.7D and -1.3D, thus smaller and opposite to the human's eye chromatic aberrations (1.75D) as we can see on Fig. 5 (in a classic photon sieve, chromatic aberrations for order 1 and -1 are respectively -0.7D and +0.7D).

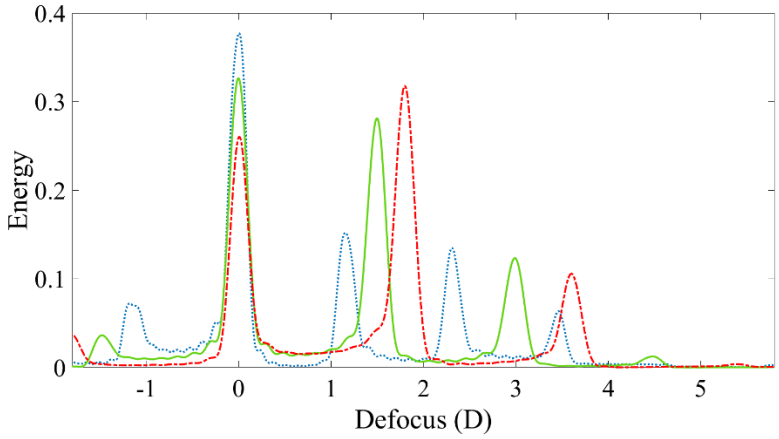

Fig. 5. Through focus energy for three wavelengths (420 nm: dotted blue line, 546 nm: solid green line, 660 nm: dashed red line). The maximum chromatic aberration of the inlay is around -1.3 diopter between 420 nm and 660 nm for the second order.

Optics EXPRESS

2.2. Implant manufacturing

In order to validate our simulations three types of implants were manufactured.

The first implant type was manufactured on a glass plate using a parallel direct-writing photolithographic technique as follows [25]. A thick layer of Microposit photoresist was deposited on a glass substrate by spin-coating. The phase profile was written into this layer with our massively parallel direct-write photo-plotter with an address grid of 750 nm and a depth resolution of few nanometers. The second type was made by UV nano-imprit duplication of the photoresist implant into ormocomp [26], a photopolymer that belongs to the class of Ormocers (organically modified ceramics) with good biocompatible properties [27]. This nano-imprint technique results in components with a residual layer of ormocer between the copied pattern and the substrate which makes it possible to validate the optical properties of the implant but not the permeability properties. In order to have a prototype on which we were able to test both the optical properties and nutrient permeability, a third and final prototype in ormocomp was manufactured using a two-photon polymerization (2PP) process [28].

Because our model of light propagation through the inlay does not consider the implant thickness, we first checked that we could correctly predict the results for a classic PS made in a 50 microns thick metal sheet. As expected, results agreed with simulations, confirming that with holes at least an order of magnitude larger than the implant's thickness, this one can be neglected.

We then also checked that we could obtain the classic PS results with one made in S1828 (545 nm thick to produce a π phase shift in air at 632 nm). Sequentially, three blazed PS prototypes were manufactured: the first in a 990 nm layer of S1828, thus producing a 2π phase shift in air at 632 nm, and another in a 2.833 µm thick layer of ormocomp for 2π phase shift when placed in water at 546 nm. The final prototype Fig. 6 was fabricated in a 3.8 µm thick ormocomp layer using the 2PP process. This thickness corresponds to a 2π phase shift between the ormocomp and the cornea. For each implant, we set w = 10%, K = 1.2 and varied the holes spacing (S).

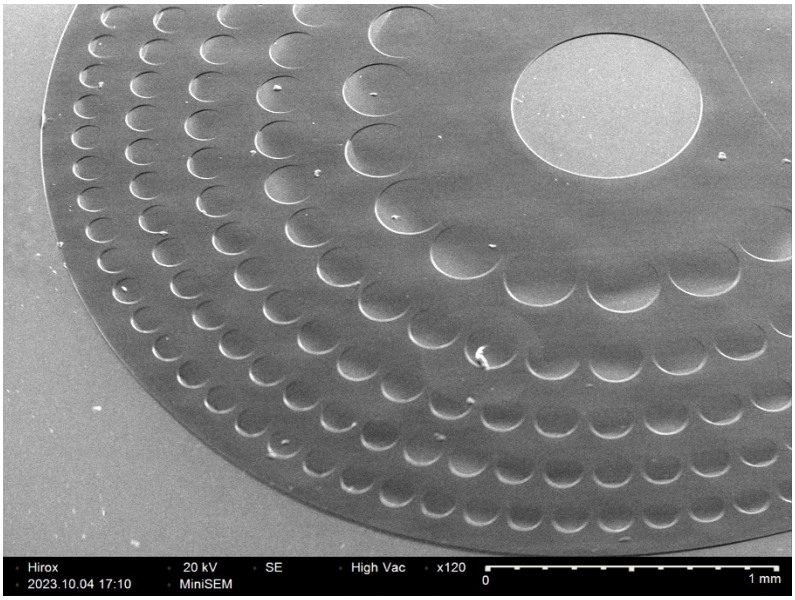

Fig. 6. MEB photography of the prototype made in an ormocomp based material with a direct writing technique. This prototype was made by a 2PP photoplotter. Inlay thickness is 3.8 µm, to induce a 2π phase shift between ormocomp and cornea. The central hole is 700 µm large in diameter and the smallest holes are 90 µm large.

Optics EXPRESS

2.3. Implant testing

In order to assess the agreement between simulations and experimental results, the through focus PSF was experimentally measured using the set-up depicted in Fig. 7 then the MTF through focus using TriOptics' OptiSpheric, an industrial control tool often referred to as a standard in implant metrology.

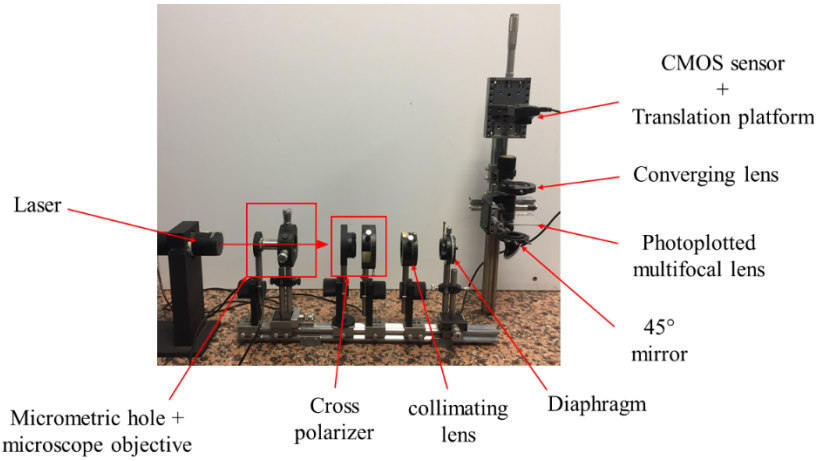

Fig. 7. Characterization set up to record energy along optical axis. The light source is a He-Ne Laser of 632 nm, spatially filtered with a x10 microscope objective and a 20 µm pinhole. The light beam is attenuated by cross polarizer, and collimated with bi convex lens. Then the light beam goes through the inlay, and a converging lens which allow to analyze the non-converging order. A CMOS sensor on a translation platform is then used to scan the optical to record the through focus PSF.

3. Results

As presented in section 2.2, in order to first validate our prototyping loop (simulation and manufacturing), we first produced standard fully transparent photon sieves with different holes density and measured the through focus PSF on our optical bench. As depicted in Fig. 8, there is a good agreement with theoretical results. The symmetry between order 1 and order -1 is visible as well as the inverse dependence of energy in the first orders with respect to the spacing between holes. For the order 0, the difference between the two curves is due to the fact that the experimental diffraction efficiency is a little lower than the theoretical one, because of manufacturing imperfections. So when holes are close to one another, the amount of energy not diffracted (dashed line) is larger than expected. For the orders -1/+1, the difference between the offset between the two curves is due to the fact that the images made for measurements are not taken in the same plane, according to the optical axis. The positive order is measured in front of the negative one, so the energy attenuation due to dispersion is smaller.

Once the prototyping loop validated, we manufactured the blazed photon sieves (as described in section 2.2) to test our innovative design. Six lenses were made with six different spacings between holes corresponding to different energy ratios between the zero and first order. Similar to Fig. 8, Fig. 9 presents the energy distribution for the three orders of interest as a function of holes spacing. Again, experimental results are in good agreement with simulations, confirming the interest of our approach to balance the energy distribution. The difference between simulation and experimentation is due to the same causes than with the classic photon sieve. For the 0 order, the fact that the amount of energy in the zero order decreases less quickly with increasing

Optics EXPRESS

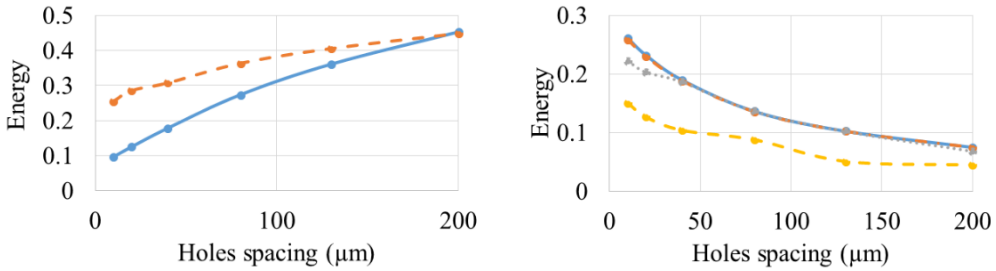

Fig. 8. Energy (ES) in the 0 order (Left) and in the first orders (Right) as a function of holes spacing (µm) in a classic photon sieve. (Left: Solid blue line represent simulations results and the dashed orange: experimental ones. Right: Superimposed solid and dash-dotted lines represent simulations results, dotted grey line represent the experimental result for the positive order and the dashed yellow line: for the negative one).

hole density than experimentally expected is due to reduced diffraction efficiency. Similarly, the difference between theoretical and experiment results for the diffractive orders, is due to dispersion. The measurement of energy for the 2nd order is done in a plane which is in front of the measurement plane of 1st order. This induces an energy offset of order 2 compared to order 1.

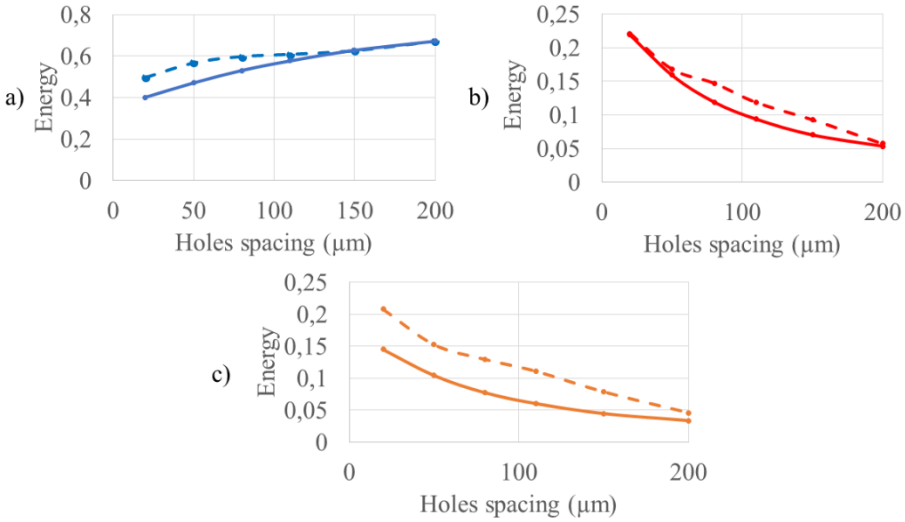

Fig. 9. Comparison of simulation and experimental results for the diffracted energy (ES) in a) order 0, b) order 1, c), order 2, as a function of holes spacing (µm) in a slanted photon sieve. Solid line represents simulation results and dashed lines the experimental ones.

In Fig. 9, the quantity of non-diffracted energy is greater than with the classic PS because with the blazed PS we operate in 2π (instead of π with the classic) this means that only the surface of the slopes participates to diffraction whereas it is the entire surface of the holes (including the central hole) in the case of classic PS.

Then, in order to analyses the optical properties of the intracorneal inlay with the same method used to analyze commercial IOLs, we used a TriOptics' OptiSpheric. This device allows us to get the through focus MTF of our inlay. Since the Trioptics is made to characterize intraocular implants (so with a power around 20D) and that our implant is afocal, a 20D IOL was placed after the inlay prototype. Measurements were carried out at 50 cc/mm and 546 nm (Optispheric uses a filtered white light source). Simulations presented in Fig. 10 were carried out with Zemax

Optics EXPRESS

and model the implant's performances in the OptiSpheric. The Zemax model of the Optishperic was provided by Trioptics, the one of the 20D IOL used was provided by Cristalens and the PS implant was modelled using grid phase surface. As depicted in Fig. 10, experimental results agree with expectations. The discrepancy between the two curves can be explained by the tendency of the Trioptics to overestimate low MTF values and the addition of the 20D IOL that led to a slight increase in spherical aberration (and thus a slightly increased depth of focus).

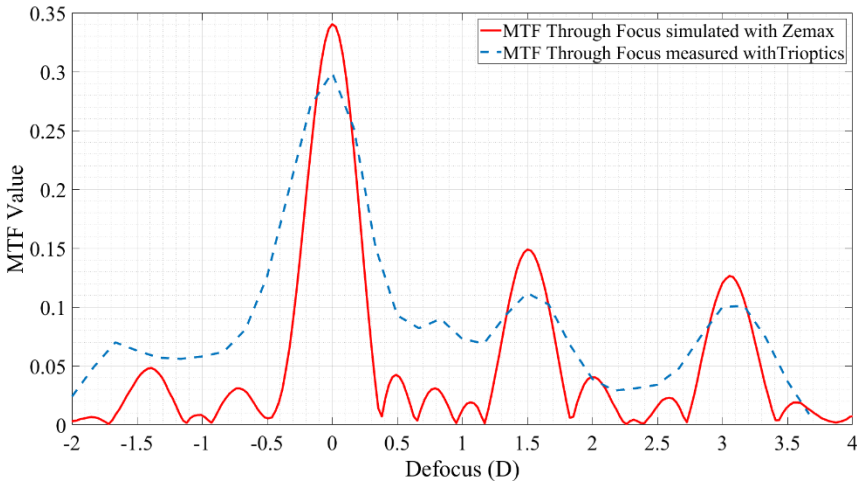

Fig. 10. Comparison of the experimental MTF at 50 cc/mm and 546 nm (dashed line) and the one simulated with Zemax (solid line). The x-axis is the defocus in diopters and y-axis the MTF value. Since the Trioptics is made to characterize intraocular implants (so with a power around 20D) and that our implant is afocal, a 20D IOL was placed after the inlay prototype. This monofocal IOL had an MTF value equal to 0.8 which explain the differences observed here between simulation and experimentation.

4. Discussion

According to our simulations and experimental results, the use of slanted holes in a photon sieve introduce a new degree of freedom that allows breaking the symmetry of light energy distribution in the diffraction orders. In this paper, we presented how such a configuration could be used to improve on existing corneal implants for the correction of presbyopia (for instance by suppressing the -1 order and distributing 60% of energy in the zero order (for far vision), and the rest in the first and second order (respectively for intermediate and near vision). This is to our knowledge, the first report of experimental results obtained with an intracorneal implant manufactured in a biocompatible material and based on the photon sieve principle.

As briefly presented in the introduction, various methods exist for the correction of presbyopia. If we focus on intracorneal implants alone, the number of solutions presented is limited and our solution compares favorably. In terms of implants using drainage holes, Furlan et al. presented a true multifocal design but without control of the energy balance between near and far vision. The Kamra is basically a pin-hole (1.6 mm in diameter) with micro-drainage holes around that extends the depth of focus but can only be placed in one eye. Implants without drainage holes include the Raindrop Near Vision Inlay and the Presbia's Flexivue Microlens that both created some multifocality by having a central zone and a peripheral one of different refractive power. These two implants were abandoned.

A number of additional tests remain to be carried out to demonstrate practically the interest of the approach. For instance, how will the holes be filled when inserted into the cornea? Or

Optics EXPRESS

could they get clogged and how their drainage property will compare with standard holes? More importantly, what will be the refractive index of the material or liquid filling the holes? As a small change in refractive index value can have a significant impact on the performances of the implant, bioreactor tests should be carried out to answer this question.

In terms of limitations, the implant presented here is not designed to correct for the patient's refractive error. Because the implant uses the zero order for far vision, varying the hole density along the radial and azimuthal coordinates would only provide some sphero-cylindrical correction at intermediate and near distance. An alternative might be to use an implant with a refractive power but its design would be far from trivial since a variable thickness also means a variable phase shift. Intracorneal implants can be placed beneath a Lasik flap, so the simplest solution may be to take advantage of the surgery to perform refractive correction. Another limitation of the current design is that it requires the development of an industrial manufacturing process. The current implant was made using photolithographic techniques as it gave us a certain flexibility in producing prototypes but other processes such as laser machining could be used.

Transparent photon sieves are advanced lenses with several interdependent parameters and the customization of the 3D hole bring yet more flexibility. In this study, only PS with circular holes were presented, but similar results could be obtained with other shapes. For instance, slanted rectangular holes could be used, as depicted in Fig. 11. Similarly, the holes radial position could also be altered with limited impact (as illustrated by the large variety of PS design in the literature).

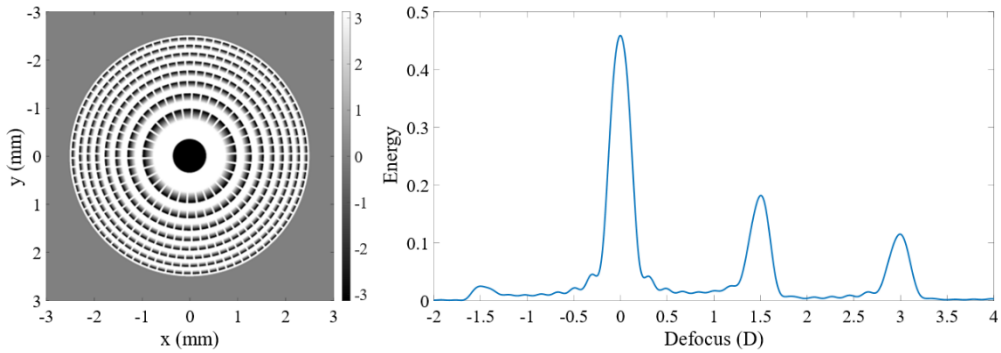

Fig. 11. Blazed photon sieve with rectangular holes (left) and associated through focus energy in a 60D eye (right). The PS thickness is chosen to produce a 2π -phase shift between the plain and holed part. In the right image, the highest peak corresponds to the light that goes through the implant without forming interference (order 0), and the following peaks correspond to the +1 and +2 order, that can be used respectively for intermediate and near vision.

The interest of the presented structure extends however further than ophthalmic applications. Fresnel Zone plates and now PS find applications in various fields from satellite imaging to microscopy [18], passing by chromatic confocal tomography [29]. The blazed PS design could be adapted to produce a different energy distribution between the different orders than the one presented here. For instance, with holes pointing inwards (rather than outwards here), the energy distribution would be opposite to the one described in Fig. 4. or Fig. 11. Also, if the necessity of through holes is removed then non-through holes of various depth could be used and with a honeycomb structure as presented in [30], a bifocal implant could be designed (Fig. 12).

In conclusion, the possibility, demonstrated in this article, of playing on the 3D profile of the hole brings a new advantage to the photon sieve structure and open yet new potential for applications where a thin, light-weight and cost-effective component is needed.

Optics EXPRESS

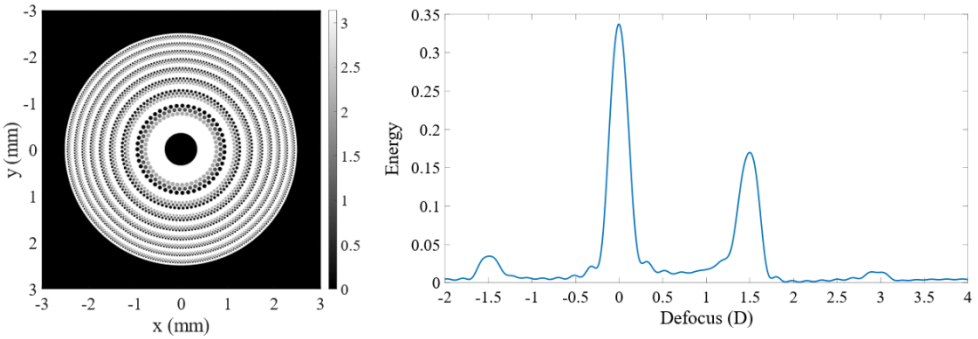

Fig. 12. Left: Holes distribution for the honeycombed photon sieve and associated through focus energy (right) in a 60D eye. The PS thickness is chosen to produce a π -phase shift between the plain and holed part. In the right image, the higher peak corresponds to the light that goes through the implant without forming interference (order 0), and the rights peaks correspond to the +1 order, that can be use respectively for intermediate or near vision.

Funding. Cristalens Industrie; Association Nationale de la Recherche et de la Technologie.

Acknowledgment. We wish to thank Prof. Kevin Heggarty for helpful advices on the manufacturing process.

Disclosures. The authors declare no conflict of interests.

Data availability. Data underlying the results presented in this paper are not publicly available at this time but may be obtained from the authors upon reasonable request.

References

1. T. R. Fricke, N. Tahhan, S. Resnikoff, *et al.*, "Global Prevalence of Presbyopia and Vision Impairment from Uncorrected Presbyopia," Ophthalmology **125**(10), 1492–1499 (2018).
2. A. Mahrous, J. B. Ciralsky, and E. C. Lai, "Revisiting monovision for presbyopia," Curr. Opin. Ophthalmol. **29**(4), 313–317 (2018).
3. C. Alvarez-Peregrina, M. A. Sanchez-Tena, M. Martin, *et al.*, "Multifocal contact lenses: A bibliometric study," J. Optom. **15**(1), 53–59 (2022).
4. T. Naujokaitis, G. U. Auffarth, R. Khoramnia, *et al.*, "Complementary system vs conventional trifocal intraocular lens: comparison of optical quality metrics and unwanted light distribution," J. Cataract. Refract. Surg. **49**(1), 84–90 (2023).
5. I. G. Pallikaris and S. I. Panagopoulou, "PresbyLASIK approach for the correction of presbyopia:," Curr. Opin. Ophthalmol. **26**(4), 265–272 (2015).
6. E. Philippaki, L. Gobin, J. Mandoda, *et al.*, "Optical evaluation of new-design multifocal IOLs with extended depth of focus," J. Opt. Soc. Am. A **36**(5), 759 (2019).
7. G. O. Waring, "Correction of Presbyopia With a Small Aperture Corneal Inlay," J. Refract. Surg. **27**(11), 842–845 (2011).
8. E. I.-H. Wu, "Review of Corneal Inlays for Presbyopia," Adv. Ophthalmol. Optom. **2**(1), 355–365 (2017).
9. M. A. Moarefi, S. Bafna, and W. Wiley, "A Review of Presbyopia Treatment with Corneal Inlays," Ophthalmol Ther. **6**(1), 55–65 (2017).
10. J. Whitman, P. J. Dougherty, G. D. Parkhurst, *et al.*, "Treatment of Presbyopia in Emmetropes Using a Shape-Changing Corneal Inlay," Ophthalmology **123**(3), 466–475 (2016).
11. W. N. Charman, "Developments in the correction of presbyopia II: surgical approaches," Ophthalmic Physiol. Opt. **34**(4), 397–426 (2014).
12. W. N. Charman, "Pinholes and presbyopia: solution or sideshow?" Ophthalmic Physiol. Opt. **39**(1), 1–10 (2019).
13. S. A. Naroo and P. S. Bilkhu, "Clinical utility of the KAMRA corneal inlay," Clin. Ophthalmol. **913**, 913 (2016).
14. S. I. Brown and S. Mishima, "The Effect of Intralamellar Water-Impermeable Membranes on Corneal Hydration," Arch. Ophthalmol. **76**(5), 702–708 (1966).
15. W. D. Furlan, D. Montagud-Martínez, V. Ferrando, *et al.*, "A new trifocal corneal inlay for presbyopia," Sci. Rep. **11**(1), 6620 (2021).
16. W. D. Furlan, S. García-Delpech, P. Udaondo, *et al.*, "Diffractive corneal inlay for presbyopia," J. Biophotonics **10**(9), 1110–1114 (2017).
17. G. O. Waring and S. D. Klyce, "Corneal Inlays for the Treatment of Presbyopia," Int. Ophthalmol. Clin. **51**(2), 51–62 (2011).
18. G. Andersen, "Large optical photon sieve," Opt. Lett. **30**(22), 2976 (2005).

Optics EXPRESS

19. L. Kipp, M. Skibowski, R. L. Johnson, *et al.*, "Sharper images by focusing soft X-rays with photon sieves," Nature **414**(6860), 184–188 (2001).
20. H.-S. Son, G. Łabuz, R. Khoramnia, *et al.*, "Laboratory analysis and ray visualization of diffractive optics with enhanced intermediate vision," BMC Ophthalmol. **21**(1), 197 (2021).
21. F. Giménez, J. A. Monsoriu, W. D. Furlan, *et al.*, "Fractal photon sieve," Opt. Express **14**(25), 11958 (2006).
22. J. Ke and J. Zhang, "Generalized Fibonacci photon sieves," Appl. Opt. **54**(24), 7278 (2015).
23. G. Andersen and D. Tullson, "Broadband antihole photon sieve telescope," Appl. Opt. **46**(18), 3706 (2007).
24. W. Sun, Y. Hu, D. G. Macdonnell, *et al.*, "Fully transparent photon sieve," 8 (n.d.).
25. M. V. Kessels, "Versatile stepper based maskless microlithography using a liquid crystal display for direct write of binary and multilevel microstructures," J. Micro/Nanolith. MEMS MOEMS **6**(3), 033002 (2007).
26. A. C. Yong, K. Heggarty, C. Carré, *et al.*, "Rapid prototyping of diffractive optical elements in microstructured sol-gel hybrid material," (2011).
27. C. Schizas and D. Karalekas, "Mechanical characteristics of an Ormocomp® biocompatible hybrid photopolymer," J. Mech. Behav. Biomed. Mater. **4**(1), 99–106 (2011).
28. C. Arnoux, L. A. Pérez-Covarrubias, A. Khaldi, *et al.*, "Understanding and overcoming proximity effects in multi-spot two-photon direct laser writing," Addit. Manuf. **49**, 102491 (2022).
29. S. L. Dobson, P. Sun, and Y. Fainman, "Diffractive lenses for chromatic confocal imaging," Appl. Opt. **36**(20), 4744 (1997).
30. M. N. Julian, D. G. MacDonnell, and M. C. Gupta, "High-efficiency flexible multilevel photon sieves by single-step laser-based fabrication and optical analysis," Appl. Opt. **58**(1), 109 (2019).